





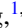









## Generation of terahertz transients from $\text{Co}_2\text{Fe}_{0.4}\text{Mn}_{0.6}\text{Si}$ -Heusler-alloy/normal-metal nanobilayers excited by femtosecond optical pulses

Sarah Heidtfeld <sup>1,2</sup> Roman Adam <sup>1,\*</sup> Takahide Kubota <sup>3,4</sup> Koki Takanashi <sup>3,4,5</sup> Derang Cao <sup>1,6</sup>  
 Carolin Schmitz-Antoniak<sup>1</sup> Daniel E. Bürgler <sup>1</sup> Fangzhou Wang <sup>1,2</sup> Christian Greb <sup>1,2</sup> Genyu Chen <sup>7,8</sup>  
 Ivan Komissarov<sup>9,10</sup> Hilde Hardtdegen <sup>11</sup> Martin Mikulics <sup>11</sup> Roman Sobolewski <sup>7,8,9,12</sup>  
 Shigemasa Suga <sup>1,13</sup> and Claus M. Schneider <sup>1,2,14</sup>

<sup>1</sup>Research Centre Jülich, Peter Grünberg Institute, 52425 Jülich, Germany

<sup>2</sup>Faculty of Physics, University of Duisburg-Essen, 47048 Duisburg, Germany

<sup>3</sup>Institute for Materials Research, Tohoku University, Sendai 980-8577, Japan

<sup>4</sup>Center for Spintronics Research Network, Tohoku University, Sendai 980-8577, Japan

<sup>5</sup>Center for Science and Innovation in Spintronics (Core Research Cluster), Tohoku University, Sendai 980-8577, Japan

<sup>6</sup>College of Physics, National Demonstration Center for Experimental Applied Physics Education, Qingdao University, Qingdao 266071, China

<sup>7</sup>Materials Science Graduate Program, University of Rochester, Rochester, New York 14627, USA

<sup>8</sup>Laboratory for Laser Energetics, University of Rochester, Rochester, New York 14623, USA

<sup>9</sup>Department of Electrical and Computer Engineering, University of Rochester, Rochester, New York 14627, USA

<sup>10</sup>Belarusian State University of Informatics and Radioelectronics, Minsk 220013, Belarus

<sup>11</sup>Research Centre Jülich, Ernst Ruska Centre for Microscopy and Spectroscopy with Electrons, 52425 Jülich, Germany

<sup>12</sup>Department of Physics and Astronomy, University of Rochester, Rochester, New York 14627, USA

<sup>13</sup>The Institute of Scientific and Industrial Research, Osaka University, Ibaraki, Osaka 567-0047, Japan

<sup>14</sup>Department of Physics, University of California Davis, Davis, California 95616, USA



(Received 26 May 2021; revised 25 August 2021; accepted 26 August 2021; published 11 October 2021)

We generated pulses of electromagnetic radiation in the terahertz (THz) frequency range by optical excitation of  $\text{Co}_2\text{Fe}_{0.4}\text{Mn}_{0.6}\text{Si}$  (CFMS)/normal-metal (NM) bilayer structures. The CFMS is a Heusler alloy showing a band gap in one spin channel and is therefore a half metal. We compared the THz emission efficiency in a systematic manner for four different CFMS/NM bilayers, where NM was either Pt, Ta, Cr, or Al. Our measurements show that the THz intensity is highest for a Pt capping. We also demonstrate the tunability of the THz amplitude by varying the magnetic field for all four bilayers. We attribute the THz generation to the inverse spin Hall effect. In order to investigate the role of the interface in THz generation, we measured the spin mixing conductance for each CFMS/NM bilayer using a ferromagnetic resonance method. We found that the spin-orbit coupling cannot completely describe the THz generation in the bilayers and that the spin transmission efficiency of the CFMS/NM interface and the spin diffusion length, as well as the oxidation of the NM layer, play crucial roles in the THz emission process.

DOI: [10.1103/PhysRevResearch.3.043025](https://doi.org/10.1103/PhysRevResearch.3.043025)

### I. INTRODUCTION

The detailed understanding of spin-to-charge conversion has been gaining paramount importance due to intended applications of the effect in low-power, high-speed spin-based electronic devices. To date, a variety of phenomena including the spin Hall effect [1,2], the spin Seebeck effect [3,4], and spin pumping [5] have been employed for the generation of spin currents. The spin Hall effect was predicted theoretically in 1971 [6] and the first experimental observation

of the inverse process was made in 1984 [7]. Since then, it has been known that the inverse spin Hall effect (ISHE) can be employed for the conversion of a spin current into a charge current in ferromagnet (FM)/normal-metal (NM) bilayer structures [7,8]. Due to the spin-orbit coupling (SOC) in the NM layer, electrons with opposite spin alignments are deflected into opposite directions and create a charge current density  $\vec{J}_c$ . The latter is related to the spin current density  $\vec{J}_s$  via

$$\vec{J}_c \propto D_{\text{ISHE}} \vec{J}_s \times \vec{\sigma}, \quad (1)$$

where  $D_{\text{ISHE}}$  is the spin Hall angle and  $\vec{\sigma}$  is the spin polarization direction of  $\vec{J}_s$  [9,10]. As demonstrated earlier [11–13], triggering this process by femtosecond laser pulses results in bursts of charge currents, leading to the emission of electromagnetic transients, which show a frequency content extending up into the terahertz (THz) frequency range. Femtosecond laser pulses impinging on the bilayer first generate mobile charge carriers. Here, *majority*-spin electrons excited

\*Corresponding author: [r.adam@fz-juelich.de](mailto:r.adam@fz-juelich.de)

Published by the American Physical Society under the terms of the [Creative Commons Attribution 4.0 International](https://creativecommons.org/licenses/by/4.0/) license. Further distribution of this work must maintain attribution to the author(s) and the published article's title, journal citation, and DOI.

into *sp* states possess a higher velocity than *minority*-spin electrons excited into *d* states and, due to their longer mean free path, they can reach the adjacent normal-metal layer [14]. Consequently, a nonzero spin current flows from the FM into the NM layer. Here, in turn, the material-specific spin-orbit coupling, leading to the spin-dependent scattering, has been singled out as the decisive factor determining the amplitude of a THz transient emitted from a dipolelike electromagnetic emitter [11].

Heusler alloys are promising candidates as materials for spintronic applications. The so-called full Heusler alloys exhibit a structure of  $A_2BC$ , where *A* and *B* stand for transition metals and *C* stands for an element from the III to V group of elements in the periodic table. Some Heusler alloys belong to half metals and are supposed to show, ideally, 100% spin polarization at the Fermi level. This is expected to result in a substantial enhancement of the polarization of spin currents. In addition, a low magnetic damping constant  $\alpha$ , characteristic for these materials [15], is a preferred parameter for spintronic devices [16,17]. Especially, cobalt-based Heusler alloys have received strong attention for device application, due to their high Curie temperature [18,19]. The magnetic damping in  $\text{Co}_2\text{Fe}_x\text{Mn}_{1-x}\text{Si}$  (CFMS) depends on the stoichiometry, especially on the amount of Fe and Mn, as has been investigated in detail in [15]. The lowest damping was found to be for  $x = 0.4$ . Hence, CFMS Heusler alloys are an extremely promising class of materials for effective spin injection and, therefore, efficient THz emitters when fabricated as CFMS/NM bilayer structures.

There are multiple physical phenomena contributing to the efficiency of THz generation in spintronic emitters. For the characterization of this process, the interface between the FM and NM layers is of great importance [20]. Spins impinging on an interface can be transmitted, be reflected, or undergo spin-flip processes due to SOC [21,22]. Such processes can be explored by the measurement of the spin diffusion lengths and the spin Hall angles. However, currently available data show a broad range of values due to different techniques and models used for the analysis [23]. The efficiency of interfacial spin transport is described by the spin mixing conductance  $g^{\uparrow\downarrow}$ . The spin current traversing the FM/NM interface decays over the spin diffusion length in the NM layer and, depending on the relation between the layer thickness and the spin diffusion length, spins can accumulate at the FM/NM interface or throughout the NM layer. In addition, the spins can get reflected not only from the FM/NM interface, but from the NM/air interface, as well. In theoretical descriptions, the latter effect is taken into account by considering the spin backflow [5,24] yielding the so-called *effective* spin mixing conductance. The latter can be extracted from ferromagnetic resonance (FMR) measurements.

In this paper, we investigate the effect of the SOC, as well as the spin transport across the CFMS/NM interface and the spin propagation in the NM material on the efficiency of the THz transient generation. We first study the static magnetic properties of our bilayers using a vibrating sample magnetometer (VSM). Second, we compare the VSM measurements with the measurements of the THz transient intensity at varying magnetic fields. In order to elucidate the role of the CFMS/NM interface, we have characterized the efficiency of

spin currents traversing the interface using FMR-induced spin pumping, from which we extracted the effective  $g^{\uparrow\downarrow}$  value. Finally, we also study the scaling of the measured THz peak amplitudes with the spin diffusion length of the NM layer and effective layer thickness, which in our sample systems is reduced due to oxidation of the NM layer.

We find that the dominant scaling of the THz generation efficiency with the SOC strength is strongly modified by the interfacial spin transmission efficiency, the spin diffusion lengths, as well as the oxidation of the NM layer, reducing the effective thickness where the ISHE takes place.

## II. MATERIALS AND METHODS

### A. Fabrication of CFMS/NM samples

The bilayer samples were fabricated onto MgO(001) single crystal substrates using an ultra-high-vacuum magnetron sputtering system with a base pressure of about  $2 \times 10^{-7}$  Pa. The stacking structure was as follows: MgO substrate/CFMS 20 nm/NM 2 nm, where the composition of the CFMS layer was  $\text{Co}_2\text{Fe}_{0.4}\text{Mn}_{0.6}\text{Si}$ , and the NM materials were Al, Cr, Ta, and Pt. The MgO substrates were preheated at 700 °C prior to the layer deposition to clean the surface and to achieve the (001) crystal plane. The deposition temperatures were 500 °C and room temperature for the CFMS layer and the NM layer, respectively.

### B. Experimental procedures

The samples were illuminated by 800-nm-wavelength and 100-fs-wide laser pulses generated by a Spectra Physics MaiTai laser oscillator. The laser beam was first split into two optical paths with a 10:90 intensity ratio. The pump beam with 90% of the intensity was used for the generation of THz radiation from our CFMS/NM bilayers. The detection of the THz radiation was achieved by a low-temperature-grown GaAs photoconductive antenna (PCA) [25–27] triggered with the 10%-intensity probe beam. Low-temperature-grown GaAs is well known for its subpicosecond ( $\approx 150$ – $300$  fs) carrier lifetime [28] which makes it suitable, besides for THz generation [29], also for detection in the THz range [30]. In order to control the time delay between the pump and probe pulses, we used a computer-controlled delay stage (DS) [see Fig. 1(a)]. After passing the DS, the pump beam was focused at a sample surface with a fluence of the order of  $6 \mu\text{J}/\text{cm}^2$  [for the fluence dependence of the THz transient generation, see Fig. 7(b) of Appendix A]. The THz radiation generated by the pump pulse was first collimated by a Teflon lens and then focused using a hemispherical Si lens (SL). The SL was placed directly in front of the PCA, which consists of two lithographically patterned metallic lines with integrated tips separated by a 6- $\mu\text{m}$  gap. The electric field of the THz radiation induces a current between the antenna tips only within the lifetime of the charge carriers excited by a probe pulse, allowing time-resolved stroboscopic sampling of the THz signal amplitude. The antenna current is first preamplified and then measured by a lock-in amplifier. The reference frequency for the lock-in was extracted from a mechanical chopper wheel, which was placed in the optical path of the pump beam. The CFMS/NM bilayers were illuminated from the NM side and the resulting THz transients emitted through the MgO substrate were

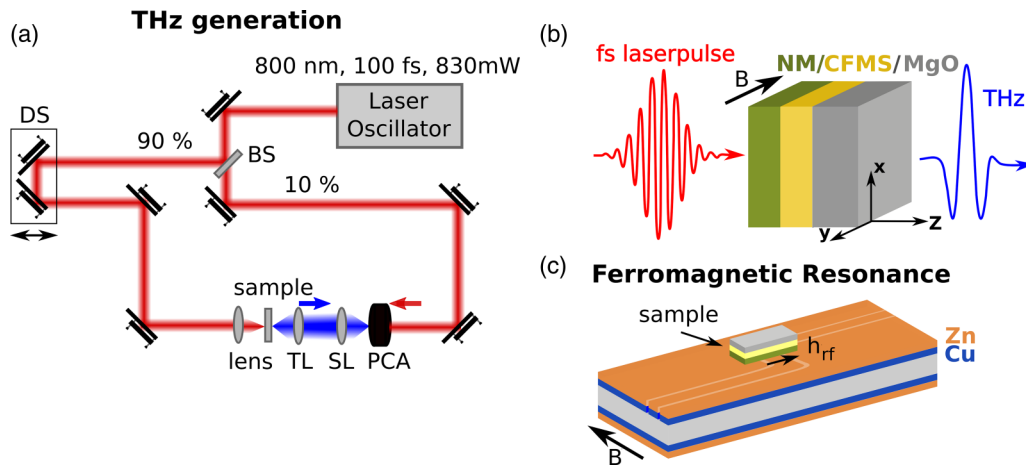


FIG. 1. Schematics of the experimental setup. (a) Laser beam paths for the generation and detection of THz radiation. (b) CFMS/NM bilayers are illuminated from the NM side and the THz signal on the MgO side is detected; the external in-plane magnetic field points along the  $y$  axis. (c) The CPW transmission line with the sample placed in the middle of the structure. The external field  $B$  is parallel and the radiofrequency (rf) field  $h_{rf}$  perpendicular to the CPW transmission line below the sample.

detected. The magnetic field was applied parallel to the sample surface and thus orthogonal to the optical axis. This geometry results in the emission of THz transients linearly polarized in the  $x$  direction [see Fig. 1(b)]. All THz measurements are performed at room temperature.

Magnetic hysteresis curves were measured by a VSM system supplied by Quantum Design. The magnetization was measured at room temperature in an in-plane configuration and the external magnetic field was tuned from  $-40$  to  $40$  kA/m.

For FMR measurements, the samples were placed on top of a coplanar waveguide (CPW) transmission line [see Fig. 1(c)]. We detected the changes of the radiofrequency (rf) signal passing through the transmission line, i.e., the  $S_{12}$  parameter, as a function of the magnetic field and frequency using a vector network analyzer [31]. The FMR transmission line consists of a  $35\text{-}\mu\text{m}$ -thick copper layer with a  $0.05\text{-}\mu\text{m}$ -thick zinc capping placed on a Rogers RO4003C board with a thickness of  $0.508$  mm, leading to a CPW impedance of  $51.32\ \Omega$ . We took frequency scans between  $50$  MHz and  $20$  GHz at a set of constant magnetic fields ranging from  $0$  up to  $160$  kA/m. The external magnetic field was applied in plane and parallel to the long axis of the transmission line [see Fig. 1(c)].

### III. RESULTS

#### A. THz transients generated from CFMS/NM bilayers

Figure 2 compiles the time- (a) and frequency-resolved (b) THz transients collected from CFMS/NM bilayers, where NM stands for a 2-nm-thick Pt, Ta, Cr, or Al capping layer [for the impact of the magnetic field direction, see Fig. 7(a) of Appendix A]. The highest THz amplitude, with the maximum intensity at  $0.69$  THz and  $-3\text{dB}$  cutoff at  $1.07$  THz, was obtained for a CFMS/Pt sample. For all other NMs, the THz maximum intensity frequency is essentially the same, while the  $-3\text{dB}$  cutoffs were  $1.00$ ,  $1.04$ , and  $1.14$  THz for CFMS/Ta, CFMS/Cr, and CFMS/Al, respectively. This observation of varying amplitudes for different NM capping layers is in agreement with literature [23] and is related to the material-

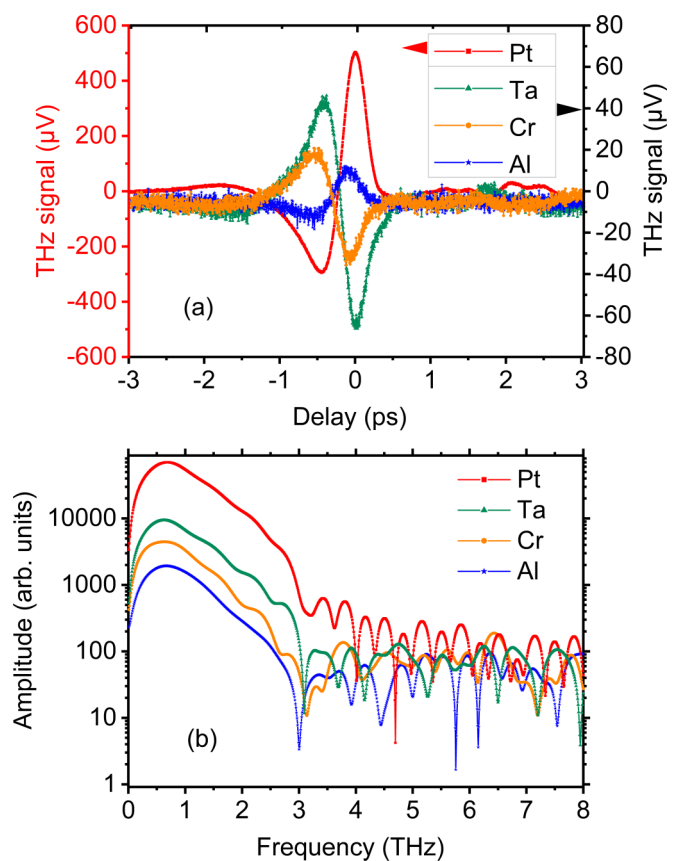


FIG. 2. Measured THz transients for CFMS/NM bilayers with NM standing for Pt, Ta, Cr, and Al (a) and corresponding FFT spectra (b). Note in (a) the different ordinate scaling for Pt (left) and Ta, Cr, Al (right). The samples were illuminated by laser pulses with a wavelength of  $\lambda = 800$  nm, pulse duration  $\tau = 100$  fs, and laser fluence of  $6\ \mu\text{J}/\text{cm}^2$ . The laser pulse was impinging at the capping layer under an angle of approximately  $5^\circ$  with respect to the surface normal. The transients are all measured in an in-plane magnetic field of  $16$  kA/m applied in the same direction.

TABLE I. Absolute [ $A^{\text{THz(meas)}}$ ] and normalized [ $A^{\text{THz(norm)}}$ ] THz amplitudes for different metallic capping materials. The  $A^{\text{THz(norm)}}$  are normalized to the THz amplitude for Pt capping  $A^{\text{THz(Pt)}}$ .  $Z^{4(\text{norm})}$  values in the fourth column were also normalized to  $Z^{4(\text{Pt})}$ .  $4\pi M_S$  values from FMR measurements represent the effective saturation magnetization of the samples. Columns 6 and 7 show damping constants  $\alpha_{\text{eff}}$  and effective spin mixing conductances  $g_{\text{eff}}^{\uparrow\downarrow}$ , respectively, both extracted from FMR measurements. Column 8 shows the spin diffusion lengths taken from the included references.

	$A^{\text{THz(meas)}} (\mu\text{V})$	$A^{\text{THz(norm)}}$	$Z^{4(\text{norm})}$	$4\pi M_S (\text{kA/m})$	$\alpha_{\text{eff}}$	$g_{\text{eff}}^{\uparrow\downarrow} (10^{18} \text{ m}^{-2})$	$\lambda_{\text{sf}} (\text{nm})$
Al	$10 \pm 2$	0.035	$7.72 \times 10^{-4}$	$1180 \pm 2$	$0.0051 \pm 0.0005$	$2.8 \pm 0.5$	490 [32]
Cr	$33 \pm 2$	0.052	0.009	$1182 \pm 3$	$0.0059 \pm 0.0003$	$3.7 \pm 0.5$	13.3 [33]
Ta	$63 \pm 2$	0.108	0.77	$1166 \pm 1$	$0.0065 \pm 0.0004$	$3.9 \pm 0.5$	1.9 [34]
Pt	$501 \pm 2$	1	1	$1191 \pm 1$	$0.0071 \pm 0.0004$	$5.2 \pm 0.7$	7.3 [34]

dependent spin Hall angle [ $D_{\text{ISHE}}$  in Eq. (1)] that leads to a difference in the spin-to-charge conversion efficiency. The spin Hall angle is determined by the material specific SOC of the NM, which scales with  $Z^4$ , where  $Z$  is the atomic number. Therefore, the highest and the lowest signal is expected for Pt and Al, respectively [2]. In Table I, we compile the measured THz amplitudes  $A^{\text{THz(meas)}}$ , as well as the normalized amplitudes  $A^{\text{THz(norm)}}$  and  $Z^4$  values, both normalized to the corresponding Pt values.

Our results are consistent with those in [12], as the inverted peaks in Fig. 2(a) reflect that Pt and Al have a reversed sign of the spin Hall angle compared to Ta and Cr.

To investigate the influence of the magnetic field on the THz generation, we measured the THz peak amplitude  $A^{\text{THz}}$  of CFMS/NM bilayers as a function of varying magnetic field for all four capping layers. Figure 3 shows the amplitude  $A^{\text{THz}}(H)$  and the magnetization  $M(H)$ , both as a function of the magnetic field  $H$ , displaying almost exactly the same hysteretic behavior. We note that all  $A^{\text{THz(norm)}}$  hystereses exhibit a substantially sharper transition between two opposite THz peak polarities, as compared to the reversal between the two antiparallel magnetization orientations measured by the VSM. We attribute this difference to a different geometry and volume of the probed samples. The VSM measurements probe

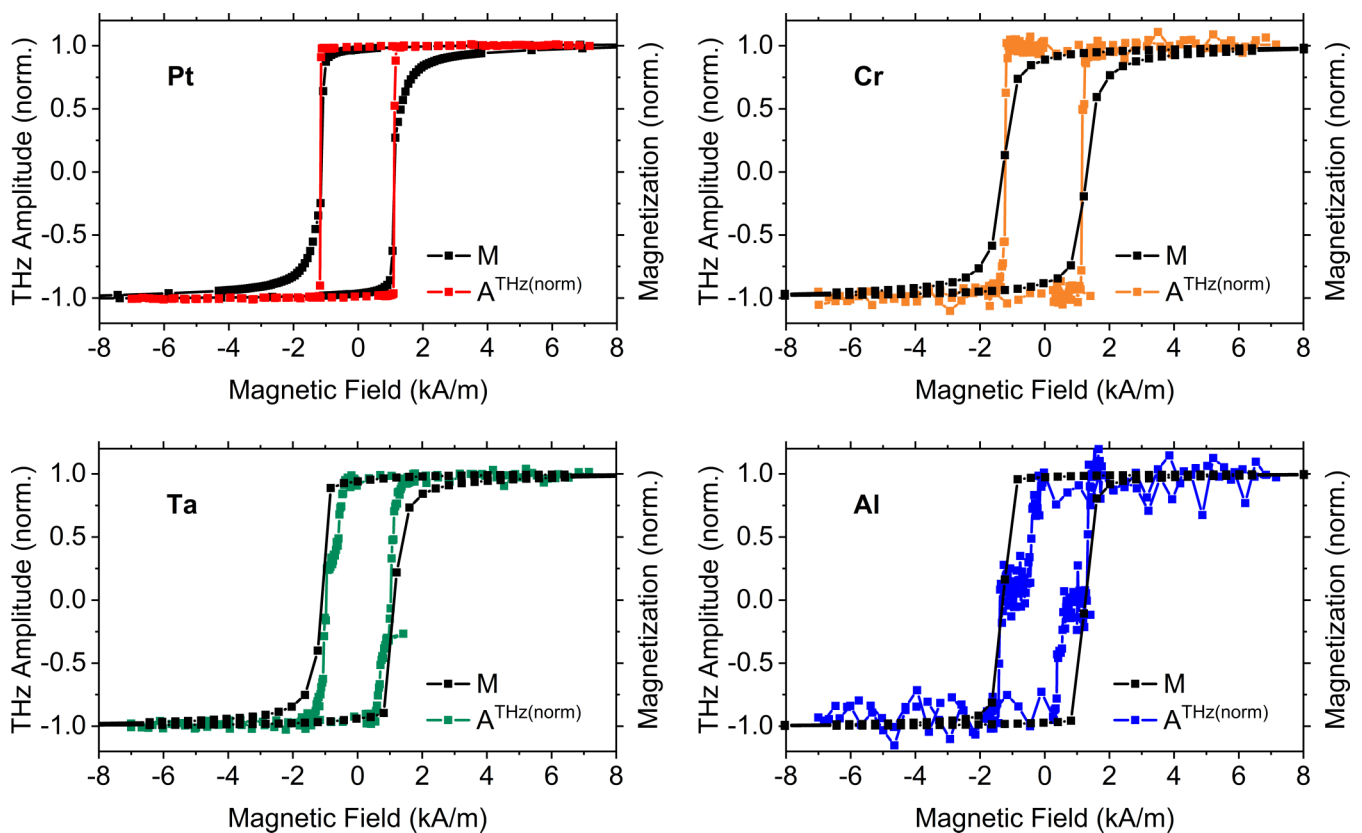


FIG. 3. Comparison of the magnetization (black symbols) and THz peak amplitude (color symbols) hystereses under variation of the external magnetic field for CFMS/NM bilayers with different NM capping materials. The diameter of the laser-beam focus spot for the THz measurements was  $200 \mu\text{m}$  ( $1/e^2$  beam waist).

the entire sample volume of the magnetic film with an area in the range of 20 to 30 mm<sup>2</sup>. In contrast, the 1/e<sup>2</sup> beam waist of a laser pulse impinging on the sample during THz measurements is about 200 μm, hence the probed area differs by two orders of magnitude. Therefore, the magnetization reversal recorded by VSM measures a magnetization averaged over all domains and domain walls, as well as all inhomogeneities of the microstructure including, e.g., crystal or magnetic defects and the roughness of the film. Furthermore, the sample edges are also included, where domain walls can be pinned, consequently smoothing out the magnetization reversal. On the other hand, THz measurements probe locally a small sample volume, which does not include the sample edges, or, e.g., pinning centers so that the effects of defects will be less pronounced, therefore resulting in a sharper transition of  $A^{\text{THz}}(H)$  compared to  $M(H)$ . The impact of the magnetic in-plane anisotropy on the  $A^{\text{THz}}(H)$  loops is shown in Fig. 8 in Appendix B.

### B. Magnetic damping

The properties of the Heusler alloy/NM interface play an essential role in the efficiency of the THz generation. The interfacial spin transport can be affected by multiple effects, including electronic structure mismatch, surface roughness, and material interdiffusion, the latter two affecting the sharpness of the interface. It was observed by Singh *et al.* that CFMS Heusler alloys capped with Pt show a high interface transparency of 84% resulting in a high spin mixing conductance [35]. The interface transparency describes the ratio of the transmitted spin-polarized electrons to all the electrons reaching the interface. Therefore, Pt appears to be a well-suited material for Heusler alloy/NM devices requiring high interface transparency.

In order to characterize the CFMS/NM interfaces and the efficiency of the injection of a spin current into a NM layer, we generated spin currents by spin pumping via ferromagnetic resonance. In this approach, the rf signal applied to the transmission line leads in the ferromagnetic CFMS layer to a driven spin precession around the direction of an external magnetic field and continuously pumps spin angular momentum into the NM layer [see Fig. 1(c)]. While localized spins are precessing, they can align the spins of the delocalized electrons. This results in an increased spin accumulation  $\delta m$  in the CFMS layer and hence to a gradient across the interface, which leads to a spin current from the CFMS into the NM layer (see Fig. 4). At the FMR resonance frequency, the absorption of the rf signal is maximal, which is reflected by an absorption dip in the frequency scan. Figure 5(a) shows a series of such absorption dips in frequency scans from 0.5 to 20 GHz, measured for various applied static magnetic fields as indicated. The increase of the resonance frequency versus the external magnetic field is shown in Fig. 5(b) as an inset. The resonance frequency  $f_{\text{res}}$  of an in-plane magnetized film in a static in-plane magnetic field  $H$  is given by the Kittel formula:

$$f_{\text{res}} = \frac{\gamma}{2\pi} \sqrt{(H_K + H)(H_K + H + 4\pi M_{\text{eff}})}, \quad (2)$$

where  $\gamma$  is the gyromagnetic ratio,  $H_K$  is the anisotropy field, and  $4\pi M_{\text{eff}}$  is the effective magnetization of the sample

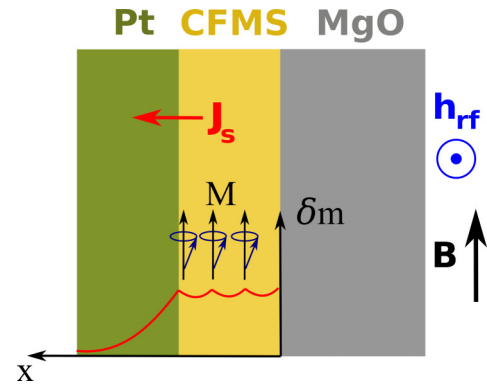


FIG. 4. Schematic sketch of spin pumping via FMR. The rf field induces precession of the localized spins in the CFMS layer around the magnetization direction  $M$ . These, in turn, are able to polarize the delocalized electrons, which leads to a spin accumulation  $\delta m$  (red curve) inside the CFMS layer. The gradient of  $\delta m$  into the Pt layer causes a spin current  $J_s$  across the interface [43].

[36]. After fitting the experimental  $f_{\text{res}}(H)$  dependence in the Fig. 5(b) inset with Eq. (2), the derivative  $\frac{\partial f_{\text{res}}(H)}{\partial H}$  can be

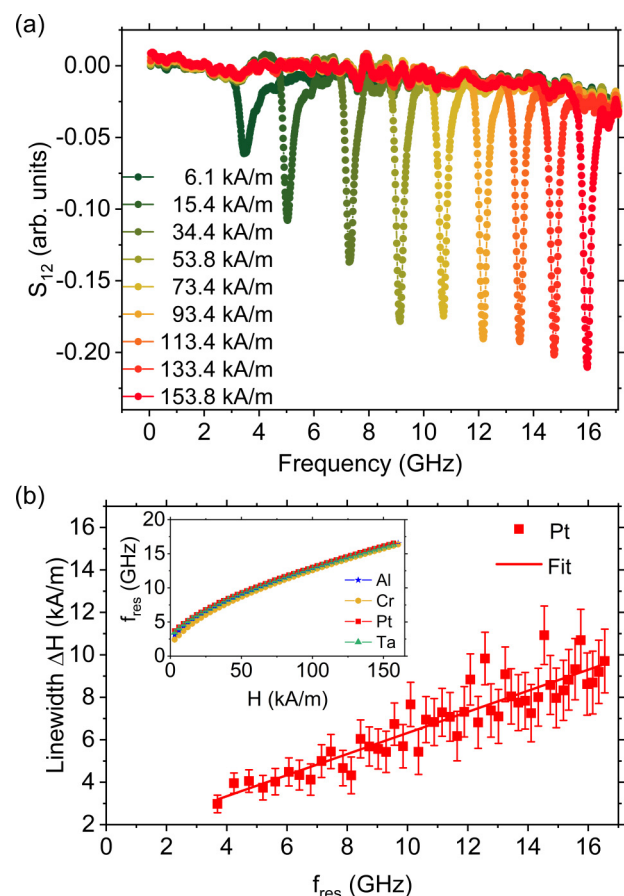


FIG. 5. (a) Frequency sweeps from 0.5 to 20 GHz with typical resonant absorption dips for several external magnetic field values. For reasons of clarity, not all measured absorption curves are shown. (b) Extracted magnetic field linewidths  $\Delta H$  calculated using Eqs. (2) and (3) vs the resonance frequencies  $f_{\text{res}}$  for Pt capping. The inset shows the increasing resonance frequency vs the external applied magnetic field for all capping layers.

calculated and allows one to convert the frequency linewidth of the resonance into the field linewidth  $\Delta H$  [37]:

$$\Delta H = \left( \frac{\partial f_{\text{res}}(H)}{\partial H} \right)^{-1} \Delta f. \quad (3)$$

We observe a linear increase of  $\Delta H$  with increasing resonance frequency  $f_{\text{res}}$ , as seen in Fig. 5(b). We included the  $\Delta H(f_{\text{res}})$  dependence for all CFMS/NM structures in Fig. 9 of Appendix C. In general,  $\Delta H(f_{\text{res}})$  can be expressed by [35,37]

$$\Delta H = \Delta H_0 + \frac{4\pi\alpha_{\text{eff}}f_{\text{res}}}{\gamma}, \quad (4)$$

where  $\Delta H_0$  is the inhomogeneous broadening, which is related to the degree of magnetic and structural inhomogeneity of the sample, and  $\alpha_{\text{eff}}$  is the effective intrinsic damping constant. We can extract  $\alpha_{\text{eff}}$  from our data by fitting the  $\Delta H(f_{\text{res}})$  dependence with Eq. (4) [see solid lines in Fig. 5(b) and in Fig. 9 of Appendix C]. In the presence of an adjacent nonmagnetic layer, the intrinsic damping constant  $\alpha_0$  of a bare CFMS film is enhanced by  $\Delta\alpha$  due to spin pumping, yielding  $\alpha_{\text{eff}} = \alpha_0 + \Delta\alpha$ . Finally, the effective spin mixing conductance  $g_{\text{eff}}^{\uparrow\downarrow}$  is related to  $\Delta\alpha$  via [35]

$$g_{\text{eff}}^{\uparrow\downarrow} = \frac{4\pi M_s t_{\text{CFMS}}}{g\mu_B} \Delta\alpha. \quad (5)$$

Here,  $t_{\text{CFMS}}$  is the thickness of the CFMS Heusler layer,  $g$  is the Landé factor, and  $\mu_B$  is the Bohr magneton. We extracted  $\alpha_{\text{eff}}$  from the experiment, as described above, and took  $\alpha_0$  from [38], where some of the present authors investigated CFMS films of the same thickness prepared by cosputtering from CoMnSi and CoFeSi targets. We stress that the effective spin mixing conductance  $g_{\text{eff}}^{\uparrow\downarrow}$  takes into account a broad range of processes contributing to spin-flip processes at the interface, as well as spin backflow of the spins arising from the reflection at the NM/air interface. The extracted damping constants  $\alpha_{\text{eff}}$  and the effective spin mixing conductances  $g_{\text{eff}}^{\uparrow\downarrow}$  for the different capping materials are listed in columns 6 and 7 in Table I. We observe the highest  $g_{\text{eff}}^{\uparrow\downarrow}$  value for the sample CFMS/Pt followed by the CFMS/Ta, CFMS/Cr, and CFMS/Al, as can be also seen in Fig. 6.

#### IV. ANALYSIS AND DISCUSSION

Below, we consider the role of spin-orbit coupling, effective spin mixing conductance, spin diffusion length, and effective NM layer thickness in the THz generation process in CFMS/NM bilayers.

To characterize the conversion efficiency of a spin current into a charge current via the ISHE, the  $D_{\text{ISHE}}$  value in Eq. (1), for the different capping materials, is a decisive parameter. It was shown in an extensive study by Wang *et al.* [34] that  $D_{\text{ISHE}}$  varies with the spin-orbit coupling and, thus, scales with  $Z^4$ . Considering the  $Z^4$  values listed in Table I, it becomes clear that CFMS/Ta and CFMS/Pt are expected to show substantially higher THz amplitudes, as compared to CFMS/Al and CFMS/Cr. In addition, the THz transients in Fig. 2 reveal that the polarity of the THz transient peak amplitudes for CFMS/Pt and CFMS/Al is opposite to that of CFMS/Ta and CFMS/Cr samples. The latter is attributed to the spin polarization at the

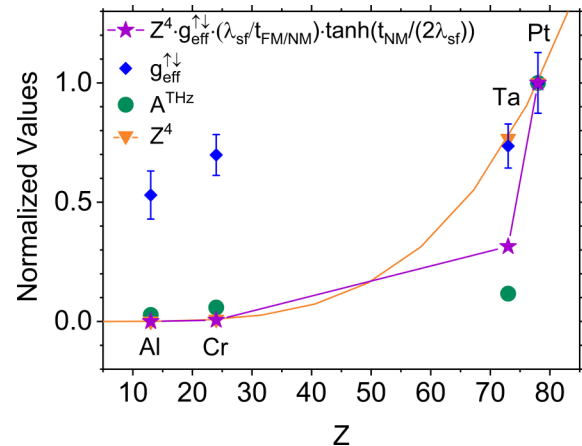


FIG. 6. Normalized THz amplitude  $A^{\text{THz(norm)}}$  (green circles),  $Z$  dependence of SOC  $Z^{4(\text{norm})}$  (yellow triangles and line), and effective spin mixing conductance  $g_{\text{eff}}^{\uparrow\downarrow(\text{norm})}$  (blue diamonds) as a function of atomic number  $Z$  for all four NM materials used as capping layers.  $Z^4$  dependence of SOC is weighted with the factors  $(\lambda_{\text{sf}}/t_{\text{FM/NM}})\tanh[t_{\text{NM}}/(2\lambda_{\text{sf}})]$  and  $g_{\text{eff}}^{\uparrow\downarrow(\text{norm})}$  (purple stars and line) to take into account the spin transmission efficiency of the CFMS/NM interfaces, the effective (nonoxidized) thickness of the NM layer, and the spin diffusion length of the different capping layers, respectively. All values of  $A^{\text{THz(norm)}}$ ,  $Z^{4(\text{norm})}$ , and  $g_{\text{eff}}^{\uparrow\downarrow(\text{norm})}$  as well as the weighted  $Z^4$  dependence are normalized to the corresponding values for the Pt capping.

Fermi level, which shows a different sign for a less-than-half or more-than-half filled  $d$  shell and is in agreement with the  $D_{\text{ISHE}}$  values reported in [23]. Figure 6 displays the THz amplitudes  $A^{\text{THz(norm)}}$  (green circles) and the  $Z^{4(\text{norm})}$  values (yellow triangles) (proportional to the spin-orbit coupling) as a function of the atomic number  $Z$ , both normalized to the Pt values. The dependences show a close agreement for Al and Cr capping; however, the amplitude  $A^{\text{THz(norm)}}$  for the Ta capping is substantially lower than expected, when considering exclusively the SOC dependence. Moreover, the FMR measurements reveal that Ta not only shows a large SOC but exhibits also a large  $g_{\text{eff}}^{\uparrow\downarrow}$  value (blue diamonds in Fig. 6). Both parameters suggest that the THz transient amplitude for CFMS/Ta should reach  $\approx 80\%$  of the amplitude of the CFMS/Pt bilayer system, which is contrary to our experiments, as is shown in Table I. The THz transient amplitude of CFMS/Ta is only  $\approx 12\%$  of the amplitude of CFMS/Pt. In order to elucidate this discrepancy, we consider the spin current propagation inside the NM layer by taking into account the spin diffusion length  $\lambda_{\text{sf}}$  of the NM material and the thickness of the bilayer system  $t_{\text{FM/NM}}$ . Literature values for  $\lambda_{\text{sf}}$  for our capping materials are included in Table I. It is immediately clear that the spin diffusion length in Ta is the shortest of all materials. It is even shorter than the nominal thickness of our Ta layer. Considering the thickness of the bilayers we took into account that the NM layers are partly oxidized, which leads to a reduction of the effective thickness of the NM layer, where the ISHE takes place. This becomes especially important for the CFMS/Ta and CFMS/Al bilayers. The thicknesses of the oxidized layers were determined by x-ray reflectivity (XRR) measurements and can be found in Fig. 10 in Appendix D. The XRR results compiled in Table II of Appendix

D indicate that approximately 2/3 of the Ta and Al capping layers are oxidized, which means that the effective thickness of the pure metallic layer is reduced for the CFMS/Ta and CFMS/Al bilayers. If we look at the dependence of the ISHE efficiency on the heavy metal (HM) layer thickness in [39,40], we see that for Ta the ISHE is maximum at approximately 2.7 nm (which equals the spin diffusion length in these references) and the efficiency of spin-to-charge conversion sharply drops for thinner films. Therefore, when comparing the results for the different sample systems, we have to take into account the different effective thicknesses of the HM layers, where the ISHE is taking place, i.e., the nonoxidized thickness of the Ta and Al layers. The Cr layer of the CFMS/Cr sample is also likely to be partially oxidized. However, no oscillation was observed in the XRR measurements of the CFMS/Cr bilayer, and consequently the nonoxidized Cr thickness could not be extracted and accounted for when comparing the different CFMS/NM bilayers.

Hence, we weighted the  $Z^4$  values, representing the material dependence of the SOC, first, by the factor  $(\lambda_{sf}/t_{FM/NM})\tanh[t_{NM}/(2\lambda_{sf})]$ , which accounts for the spin diffusion length in the NM material and the effective NM layer thickness as in [41], and, second, by the factor  $g_{eff}^{\uparrow\downarrow}$ , which takes the spin transmission efficiency of the CFMS/NM interface into account.  $t_{FM/NM}$  is the total thickness of the metal film, i.e., the thickness of the CFMS layer plus the effective, nonoxidized NM thickness  $t_{NM}$ . The comparison

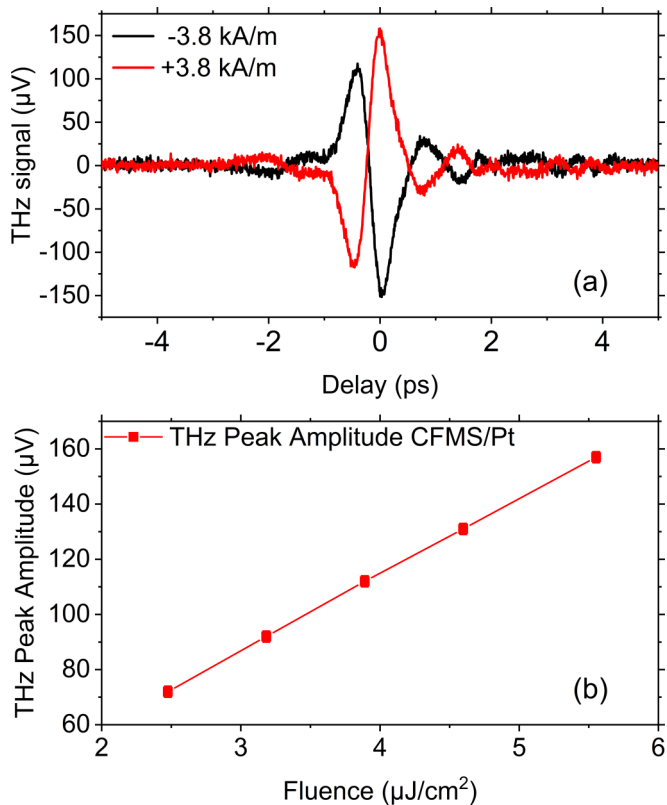


FIG. 7. (a) THz transients for CFMS/Pt taken at opposed in-plane magnetic field directions. (b) THz peak amplitude vs the fluence at the sample position for the CFMS/Pt bilayer.

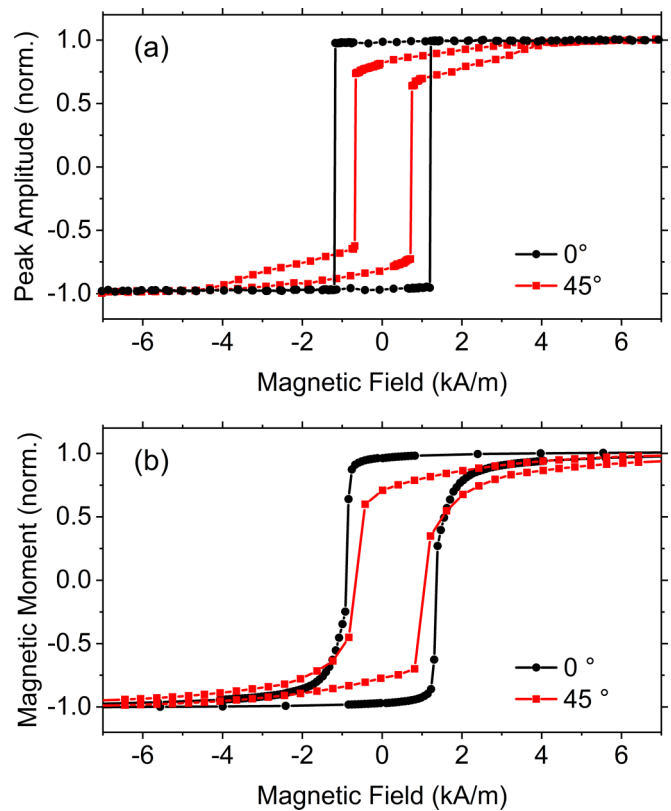


FIG. 8. (a) Hysteresis loops  $A^{THz}(H)$  of the peak amplitude of THz transients measured with the external field applied at  $0^\circ$  and  $45^\circ$  for CFMS/Pt. (b) Magnetic hysteresis loops  $M(H)$  measured by VSM with the external field applied at  $0^\circ$  and  $45^\circ$  also for CFMS/Pt.

of the weighted  $Z^4$  values (purple stars and line) with the normalized THz amplitudes (green circles) is presented in Fig. 6 and clearly shows, as expected, that the weighted value for Ta is closer to the experimental  $A^{THz(norm)}$  for CFMS/Ta.

Our analysis reveals that the SOC is not the only parameter affecting the THz transients, but  $\lambda_{sf}$ , the effective  $t_{NM}$ , and  $g_{eff}^{\uparrow\downarrow}$  must also be taken into account when describing THz generation in CFMS/NM bilayers. The small remaining discrepancy in the case of the Ta capping suggests that additional processes may still be part of the full physical picture.

On the other hand, and interestingly enough, although the SOC for Al is very low, only 0.07% of the Pt value, we observed a THz signal for a CFMS/Al bilayer with the amplitude of approximately 3% of  $A^{THz(Pt)}$ , i.e., two orders of magnitude larger than expected. In order to explore the possible reason for this surprisingly large THz amplitude for Al capping, we studied the magnetic and structural properties near the interface regions of all bilayers using x-ray absorption near-edge structure (XANES) and x-ray circular magnetic dichroism (XMCD). XANES spectra of the Mn absorption lines in Fig. 11 in Appendix E show several side peaks for the sample with Al as the capping NM material that are not present for the other capping layers. These side peaks indicate a more localized condition of the Mn 3d electrons in the CFMS/Al bilayer, which is caused by interdiffusion of Al atoms into the CFMS interface region. In [41,42], THz signals from FM/NM

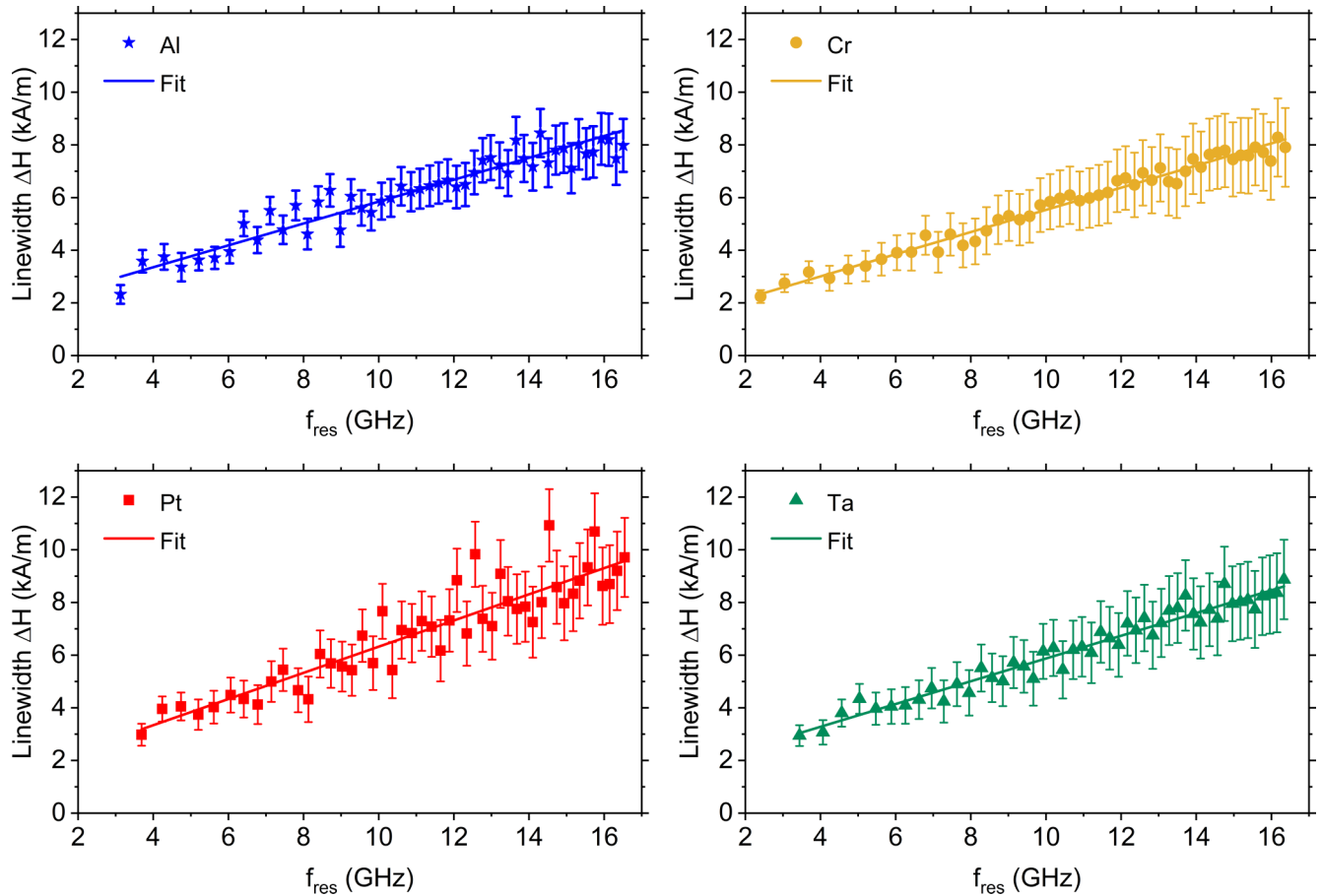


FIG. 9. FMR field linewidths  $\Delta H$  vs the resonance frequencies  $f_{\text{res}}$  for all capping materials. The solid lines are fits with Eq. (4) of the main text.

bilayers were investigated for different interface properties. It was found that the THz signal amplitudes were increased for annealed samples, which was attributed to the increased interdiffusion in the interfacial region. The counterintuitive increase of the signal amplitude has been explained by skew scattering within the interdiffusion layer, which leads to the deflection of majority-spin and minority-spin electrons into opposite directions. Although this additional skew scattering process reduces the overall spin current density in the NM layer, a stronger ISHE and thus larger amplitudes of the THz transients are observed.

## V. CONCLUSION

We have demonstrated the emission of THz transient radiation from bilayers formed by 20 nm of the half-metallic Heusler alloy  $\text{Co}_2\text{Fe}_{0.4}\text{Mn}_{0.6}\text{Si}$  capped with 2-nm-thick metallic layers of either Pt, Ta, Cr, or Al. Experimental signatures, such as the magnetic field dependence (see Figs. 3 and 7 in Appendix A), point directly to the ISHE as the mechanism of THz generation. The evolution of the THz transient amplitude with the external magnetic field follows the magnetic hysteresis loop very closely and allows the tuning of the THz amplitude and polarization by manipulating the magnetization amplitude and orientation inside the sample with an external field.

Our measurements revealed that the highest THz transient amplitude is generated by CFMS/Pt bilayers due to the largest spin-orbit coupling in Pt. The THz amplitudes of the other bilayers decrease in the order expected according to the  $Z^4$  scaling of the SOC. Nonetheless, our investigations show substantial discrepancies between the measured and expected  $Z^4$  scaling of THz amplitudes in the case of Ta and Al capping layers. In order to gain much more comprehensive insight into the physical processes affecting the THz transient generation efficiency, we first focused on the role of the CFMS/NM interface by evaluating the effective spin mixing conductance  $g_{\text{eff}}^{\uparrow\downarrow}$ , which specifies the efficiency of the interfacial spin transport. Although CFMS/Ta shows a strong SOC and a large  $g_{\text{eff}}^{\uparrow\downarrow}$ , unexpectedly it exhibits the low value of  $A^{\text{THz(Ta)}} \approx 0.1 A^{\text{THz(Pt)}}$ . We show that the influence of the spin diffusion length in CFMS/Ta is small and ascribe the low THz transient peak amplitude to the oxidation of the Ta layer, which reduces the effective thickness of the Ta layer. In contrast to the CFMS/Ta bilayer, for which we measured a THz amplitude lower than expected based on  $Z^4$  scaling of the SOC, we observed that the THz amplitude for CFMS/Al bilayers exceeds the expected value by two orders of magnitude, which we, based on XANES measurements, attribute to elemental interdiffusion at the interface. The effects considered—reduced effective NM thickness due to oxidation, spin diffusion lengths of the NM layers, and interfacial interdiffusion leading to increased



skew scattering—are not necessarily independent and can in total result in either suppression or enhancement of the THz transient signal. Further investigations of the interface characteristics as well as thickness-dependent studies can improve the overall understanding of the efficiency of THz transient generation from FM/NM multilayers.

**ACKNOWLEDGMENTS**

The work at the Research Center Jülich was performed within Jülich Short-Pulse Particle Acceleration and Radiation Center, a strategy project funded by the Bundesministerium für Bildung und Forschung (Federal Ministry of Education and Science, Germany). Research in Rochester was funded in part by National Science Foundation Grant No. #1842712.

**APPENDIX A: THZ EMISSION CHARACTERISTICS**

We observed a flip of THz polarity when reversing the applied in-plane magnetic field direction, which is a characteristic behavior for THz transients generated by the ISHE, due to reversed spin polarization in Eq. (1) of the main text [see Fig. 7(a)]. Additionally, we observed a linear scaling of the THz amplitude with the laser fluence at the sample position as shown in Fig. 7(b).

**APPENDIX B: MAGNETIC ANISOTROPY**

We measured the hysteresis loops of a CFMS/Pt sample with the magnetic field applied at an azimuthal angle of 0° and 45° by VSM and compared them with the hysteresis of the THz transient amplitudes measured with the magnetic field applied at the same angles (see Fig. 8). In both cases, we observe an easy-axis loop at 0° and the behavior of an intermediate hard axis loop at 45°.

**APPENDIX C: FERROMAGNETIC RESONANCE**

From ferromagnetic resonance experiments, we extracted the magnetic field linewidth  $\Delta H$  of the resonance, as explained in the main text. The  $\Delta H$  scales linearly with the resonance frequency  $f_{res}$ . We used Eq. (4) of the main text to fit the  $\Delta H(f_{res})$  data points and extracted the effective damping constant  $\alpha_{eff}$ . The  $\Delta H(f_{res})$  dependences and the linear fits are shown in Fig. 9 for all our CFMS/NM bilayers.

**APPENDIX D: X-RAY REFLECTIVITY MEASUREMENTS**

To investigate the thickness of the NM layers we performed XRR measurements on the CFMS/Pt, CFMS/Ta, and CFMS/Al bilayers. The obtained results and fits with the software GlobalFit by Rigaku Corp. [44,45] can be found in Fig. 10. In the XRR fitting procedure we assumed that the Ta and Al layers are composed of a pure metallic layer plus a corresponding layer of a metal oxide. The results indicate the presence of a TaO as well as an AlO oxide layer. The thicknesses of the oxidized and nonoxidized parts of the layers are listed in Table II. The XRR results also indicate some deviation from the target thickness of 2 nm. The total thicknesses of Pt, Ta-TaO, and Al-AlO capping layers were in reality 2.2,

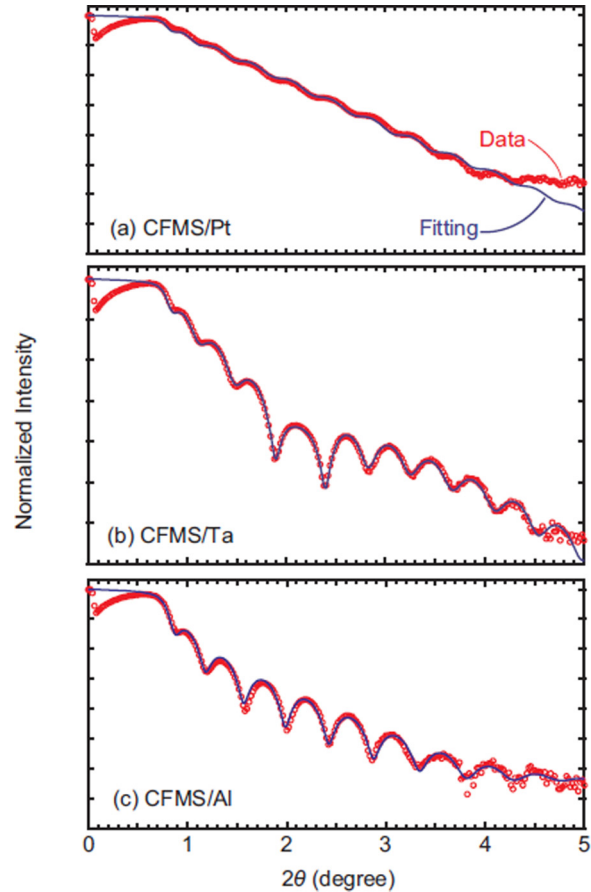


FIG. 10. XRR results (red) and fits (blue) for (a) CFMS/Pt, (b) CFMS/Ta-TaO, and (c) CFMS/Al-AIO layer systems.

3.5, and 0.5 nm, respectively. The deviations from the nominal values may be due to errors in the calibration of the deposition rates (especially critical for layer thicknesses in the range of a

TABLE II. XRR fitting parameters for the CFMS/Pt, CFMS/Ta-TaO, and CFMS/Al-AIO layers. For the bilayers with Al and Ta the NM layers are assumed to be composed of a pure layer and an oxidized layer. The table shows the thickness of the layers in nm, as well as the used density and roughness of the layers.

	Thickness (nm)	Density (g/cm <sup>3</sup> )	Roughness (nm)
CFMS/Pt			
MgO substrate		3.58463	0.82
CFMS	18.7	7.49	1.13
Pt	2.2	20.3	0.73
CFMS/Ta			
MgO substrate		3.58463	0.67
CFMS	18.6	7.52	1.56
Ta	1.2	15.4	0.61
TaO	2.3	7.6	0.85
CFMS/Al			
MgO substrate		3.58463	0.84
CFMS	19.3	7.6	0.6
Al	0.3	2.5	0.1
AlO	0.2	3.4	2.0

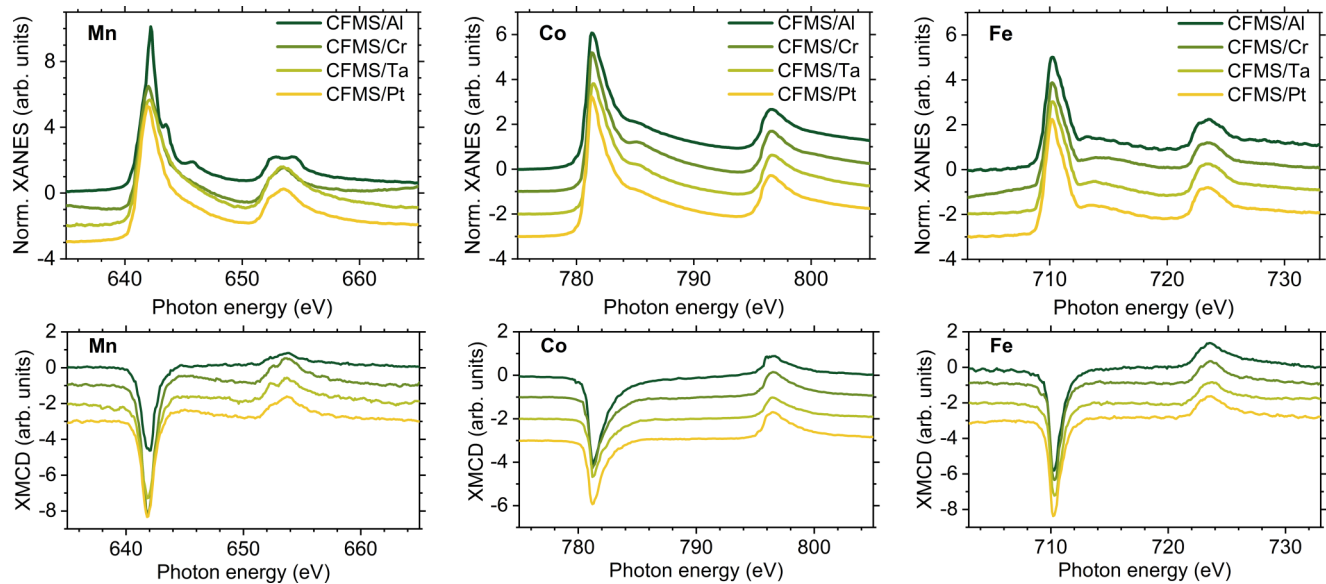


FIG. 11. XANES (top row) and XMCD (bottom row) spectra for the element-sensitive investigation of structural and magnetic properties of the CFMS close to the interfaces with the Al, Cr, Ta, and Pt capping layers (dark to light color line).

few nanometers) and, for Al and Ta, due to a volume change upon oxidation. We note that although the XRR fitting for the CFMS/Al-AIO sample is not perfect, we are confident that the estimated thicknesses can be considered reliable, because the oscillation period is reproduced. The deviations from the fitting may be due to the inhomogeneity of the AIO layer, which cannot be explained by a single and constant value of the density.

#### APPENDIX E: XANES AND XCMD INVESTIGATIONS

To study the structural and magnetic properties of a CFMS Heusler alloy near the interface to the NM, XANES and XMCD measurements were performed at BESSY II [46,47] in the experimental “ALICE” chamber of the PM3 beamline [48,49]. The measurements were performed at 300 K in reflection with  $20^\circ$  grazing incidence angle, allowing a probing depth of approximately 2 nm at 300 K. The degree of circular

polarization was 92% and the energy resolution was 0.14 eV at the Fe edge. The maximum field applied to the sample was 27 mT, and the XMCD results, shown in Fig. 11, were retrieved from the subtraction of spectra at positive and negative fields. The spectra suffer from saturation effects which become more pronounced for heavy elements. The spectra have been shifted vertically for better visibility and a saturation correction is included. We can see a large increase in the XMCD at the Mn absorption edge from Al to Cr, and only very small increase between the Ta and Pt. This only small difference can be due to the saturation effects. From the Mn XANES spectra it is evident that the Al-capped sample shows more localized  $3d$  states compared with spectra of Cr, Ta, and Pt. Several small satellite peaks next to the  $L_3$  peak at about 642 eV are clearly visible. In contrast, Co and Fe XANES spectra show a similar structure for all capping layers. The more localized Mn  $3d$  states in the Al-capped sample indicate interdiffusion of Al atoms into the CFMS layer.

- [1] J. E. Hirsch, Spin Hall Effect, *Phys. Rev. Lett.* **83**, 1834 (1999).
- [2] T. Tanaka, H. Kontani, M. Naito, D. S. Hirashima, K. Yamada, and J. Inoue, Intrinsic spin Hall effect and orbital Hall effect in  $4d$  and  $5d$  transition metals, *Phys. Rev. B* **77**, 165117 (2008).
- [3] H. Adachi, K.-i. Uchida, E. Saitoh, and S. Maekawa, Theory of the spin Seebeck effect, *Rep. Prog. Phys.* **76**, 036501 (2013).
- [4] K. Uchida, S. Takahashi, K. Harii, J. Ieda, W. Koshibae, K. Ando, S. Maekawa, and E. Saitoh, Observation of the spin Seebeck effect, *Nature (London)* **455**, 778 (2008).
- [5] Y. Tserkovnyak, A. Brataas, and G. E. W. Bauer, Spin pumping and magnetization dynamics in metallic multilayers, *Phys. Rev. B* **66**, 224403 (2002).
- [6] M. I. Dyakonov and V. I. Perel, Current-induced spin orientation of electrons in semiconductors, *Phys. Lett. A* **35**, 459 (1971).
- [7] A. A. Bakun, B. P. Zakharchenya, A. A. Rogachev, M. N. Tkachuk, and V.G. Fleisher, Observation of a surface photocurrent caused by optical orientation of electrons in a semiconductor, *JETP Lett.* **40**, 1293 (1984).
- [8] K. Ando, S. Takahashi, J. Ieda, Y. Kajiwara, H. Nakayama, T. Yoshino, K. Harii, Y. Fujikawa, M. Matsuo, S. Maekawa *et al.*, Inverse spin-Hall effect induced by spin pumping in metallic system, *J. Appl. Phys.* **109**, 103913 (2011).
- [9] E. Saitoh, M. Ueda, H. Miyajima, and G. Tatara, Conversion of spin current into charge current at room temperature: Inverse spin-Hall effect, *Appl. Phys. Lett.* **88**, 182509 (2006).
- [10] R. Yu, B. F. Miao, L. Sun, Q. Liu, J. Du, P. Omelchenko, B. Heinrich, Mingzhong Wu, and H. F. Ding, Determination of spin Hall angle and spin diffusion length in  $\beta$ -phase-dominated tantalum, *Phys. Rev. Materials* **2**, 074406 (2018).
- [11] T. Kampfrath, M. Battiato, P. Maldonado, G. Eilers, J. Nötzold, S. Mährlein, V. Zbarsky, F. Freimuth, Y. Mokrousov, S. Blügel *et al.*, Terahertz spin current pulses controlled by magnetic heterostructures, *Nat. Nanotechnol.* **8**, 256 (2013).

- [12] T. Seifert, S. Jaiswal, U. Martens, J. Hannegan, L. Braun, P. Maldonado, F. Freimuth, A. Kronenberg, J. Henrizi, I. Radu *et al.*, Efficient metallic spintronic emitters of ultrabroadband terahertz radiation, *Nat. Photonics* **10**, 483 (2016).
- [13] R. Adam, G. Chen, D. E. Bürgler, T. Shou, I. Komissarov, S. Heitfeld, H. Hardtdegen, M. Mikulics, C. M. Schneider, and R. Sobolewski, Magnetically and optically tunable terahertz radiation from Ta/NiFe/Pt spintronic nanolayers generated by femtosecond laser pulses, *Appl. Phys. Lett.* **114**, 212405 (2019).
- [14] M. Battiato, K. Carva, and P. M. Oppeneer, Superdiffusive Spin Transport as a Mechanism of Ultrafast Demagnetization, *Phys. Rev. Lett.* **105**, 027203 (2010).
- [15] T. Kubota, S. Tsunegi, M. Oogane, S. Mizukami, T. Miyazaki, H. Naganuma, and Y. Ando, Half-metallicity and Gilbert damping constant in  $\text{Co}_2\text{Fe}_x\text{Mn}_{1-x}\text{Si}$  Heusler alloys depending on the film composition, *Appl. Phys. Lett.* **94**, 122504 (2009).
- [16] L. Flacke, L. Liensberger, M. Althammer, H. Huebl, S. Geprägs, K. Schultheiss, A. Buzdakov, T. Hula, H. Schultheiss, E. R. J. Edwards *et al.*, High spin-wave propagation length consistent with low damping in a metallic ferromagnet, *Appl. Phys. Lett.* **115**, 122402 (2019).
- [17] B. Balke, G. H. Fecher, H. C. Kandpal, C. Felser, K. Kobayashi, E. Ikenaga, J.-J. Kim, and S. Ueda, Properties of the quaternary half-metal-type Heusler alloy  $\text{Co}_2\text{Mn}_{1-x}\text{Fe}_x\text{Si}$ , *Phys. Rev. B* **74**, 104405 (2006).
- [18] B. Venkateswarlu, P. V. Midhunlal, P. D. Babu, and N. H. Kumar, Magnetic and anomalous electronic transport properties of the quaternary Heusler alloys  $\text{Co}_2\text{Ti}_{1-x}\text{Fe}_x\text{Ge}$ , *J. Magn. Mater.* **407**, 142 (2016).
- [19] S. J. Ahmed, C. Boyer, and M. Niewczas, Magnetic and structural properties of  $\text{Co}_2\text{MnSi}$  based Heusler compound, *J. Alloys Compd.* **781**, 216 (2019).
- [20] W. Zhang, W. Han, X. Jiang, S.-H. Yang, and S. S. P. Parkin, Role of transparency of platinum-ferromagnet interfaces in determining the intrinsic magnitude of the spin Hall effect, *Nat. Phys.* **11**, 496 (2015).
- [21] K. Dolui and B. K. Nikolić, Spin-memory loss due to spin-orbit coupling at ferromagnet/heavy-metal interfaces: *Ab initio* spin-density matrix approach, *Phys. Rev. B* **96**, 220403(R) (2017).
- [22] W.-T. Lu, Y. Zhao, M. Battiato, Y. Wu, and Z. Yuan, Interface reflectivity of a superdiffusive spin current in ultrafast demagnetization and terahertz emission, *Phys. Rev. B* **101**, 014435 (2020).
- [23] A. Hoffmann, Spin Hall effects in metals, *IEEE Trans. Magn.* **49**, 5172 (2013).
- [24] Y. Tserkovnyak, A. Brataas, and G. E. W. Bauer, Enhanced Gilbert Damping in Thin Ferromagnetic Films, *Phys. Rev. Lett.* **88**, 117601 (2002).
- [25] M. Tani, S. Matsuura, K. Sakai, and S.-i. Nakashima, Emission characteristics of photoconductive antennas based on low-temperature-grown GaAs and semi-insulating GaAs, *Appl. Opt.* **36**, 7853 (1997).
- [26] Y. Cai, I. Brener, J. Lopata, J. Wynn, L. Pfeiffer, J. B. Stark, Q. Wu, X. C. Zhang, and J. F. Federici, Coherent terahertz radiation detection: Direct comparison between free-space electro-optic sampling and antenna detection, *Appl. Phys. Lett.* **73**, 444 (1998).
- [27] N. Vieweg, M. Mikulics, M. Scheller, K. Ezdi, R. Wilk, H. W. Hübers, and M. Koch, Impact of the contact metallization on the performance of photoconductive THz antennas, *Opt. Express* **16**, 19695 (2008).
- [28] R. Adam, M. Mikulics, A. Förster, J. Schelten, M. Siegel, P. Kordoš, X. Zheng, S. Wu, and R. Sobolewski, Fabrication and subpicosecond optical response of low-temperature-grown GaAs freestanding photoconductive devices, *Appl. Phys. Lett.* **81**, 3485 (2002).
- [29] R. Adam, M. Mikulics, S. Wu, X. Zheng, M. Marso, I. Camara, F. Siebe, R. Güsten, A. Foerster, P. Kordos *et al.*, Fabrication and performance of hybrid photoconductive devices based on freestanding LT-GaAs, in *Integrated Optoelectronic Devices 2004* (SPIE, San Jose, CA, United States, 2004).
- [30] N. M. Burford and M. O. El-Shenawee, Review of terahertz photoconductive antenna technology, *Opt. Eng.* **56**, 010901 (2017).
- [31] O. Yalcin, *Ferromagnetic Resonance Theory and Applications* (InTech, Rijeka, Croatia, 2013).
- [32] S. O. Valenzuela and M. Tinkham, Direct electronic measurement of the spin Hall effect, *Nature (London)* **442**, 176 (2006).
- [33] C. Du, H. Wang, F. Yang, and P. C. Hammel, Systematic variation of spin-orbit coupling with *d*-orbital filling: Large inverse spin Hall effect in 3d transition metals, *Phys. Rev. B* **90**, 140407(R) (2014).
- [34] H. Wang, C. Du, Y. Pu, R. Adur, P. Hammel, and F. Yang, Scaling of Spin Hall Angle in 3d, 4d, and 5d Metals from  $\text{Y}_3\text{Fe}_5\text{O}$ /Metal Spin Pumping, *Phys. Rev. Lett.* **112**, 197201 (2014).
- [35] B. B. Singh, K. Roy, P. Gupta, T. Seki, K. Takanashi, and S. Bedanta, High spin mixing conductance and spin interface transparency at the interface of a  $\text{Co}_2\text{Fe}_{0.4}\text{Mn}_{0.6}\text{Si}$  Heusler alloy and Pt, *NPG Asia Mater.* **13**, 9 (2021).
- [36] C. Kittel, On the theory of ferromagnetic resonance absorption, *Phys. Rev.* **73**, 155 (1948).
- [37] S. S. Kalarickal, P. Krivosik, M. Wu, C. E. Patton, M. L. Schneider, P. Kabos, T. J. Silva, and J. P. Nibarger, Ferromagnetic resonance linewidth in metallic thin films: Comparison of measurement methods, *J. Appl. Phys.* **99**, 093909 (2006).
- [38] S. Pan, T. Seki, K. Takanashi, and A. Barman, Ultrafast demagnetization mechanism in half-metallic Heusler alloy thin films controlled by the Fermi level, *Phys. Rev. B* **101**, 224412 (2020).
- [39] J. Liu, T. Ohkubo, S. Mitani, K. Hono, and M. Hayashi, Correlation between the spin Hall angle and the structural phases of early 5d transition metals, *Appl. Phys. Lett.* **107**, 232408 (2015).
- [40] S.-I. Kim, D.-J. Kim, M.-S. Seo, M.-S. Seo, B.-G. Park, and S.-Y. Park, Dependence of inverse-spin Hall effect and spin-rectified voltage on tantalum thickness in Ta/CoFeB bilayer structure, *Appl. Phys. Lett.* **106**, 032409 (2015).
- [41] T. S. Seifert, N. M. Tran, O. Gueckstock, S. M. Rouzegar, L. Nadvornik, S. Jaiswal, G. Jakob, V. V. Temnov, M. Mnzenberg, M. Wolf *et al.*, Terahertz spectroscopy for all-optical spintronic characterization of the spin-Hall-effect metals Pt, W and  $\text{Cu}_{80}\text{Ir}_{20}$ , *J. Phys. D* **51**, 364003 (2018).
- [42] S. Kaneta-Takada, M. Yamada, S. Sato, S. Arai, L. D. Anh, K. Hamaya, and S. Ohya, Enhancement of the Spin Hall Angle by Interdiffusion of Atoms in  $\text{CoFeAl}_{0.5}\text{Si}_{0.5}/n\text{-Ge}$  Heterostructures, *Phys. Rev. Appl.* **14**, 024096 (2020).

- [43] S. Takahashi, Physical principles of spin pumping, in *Handbook of Spintronics*, edited by Y. Xu, D. D. Awschalom, and J. Nitta (Springer, New York, Netherlands, Dordrecht, 2016), pp. 1445–1480.
- [44] L. G. Parratt, Surface studies of solids by total reflection of x-rays, *Phys. Rev.* **95**, 359 (1954).
- [45] S. K. Sinha, E. B. Sirota, S. Garoff, and H. B. Stanley, X-ray and neutron scattering from rough surfaces, *Phys. Rev. B* **38**, 2297 (1988).
- [46] T. Kachel, The PM3 beamline at BESSY II, *JLSRF* **2**, A48 (2016).
- [47] T. Kachel, F. Eggenstein, and R. Follath, A soft x-ray plane-grating monochromator optimized for elliptical dipole radiation from modern sources, *J. Synchrotron Radiat.* **22**, 1301 (2015).
- [48] R. Abrudan, F. Brüßing, R. Salikhov, J. Meermann, I. Radu, H. Ryll, F. Radu, and H. Zabel, ALICE—An advanced reflectometer for static and dynamic experiments in magnetism at synchrotron radiation facilities, *Rev. Sci. Instrum.* **86**, 063902 (2015).
- [49] R. Abrudan and F. Radu, ALICE: A diffractometer/reflectometer for soft x-ray resonant magnetic scattering at BESSY II, *JLSRF* **2**, A69 (2016).